nature communications

Article

https://doi.org/10.1038/s41467-025-57612-0

Synthesis of crystalline two-dimensional conjugated polymers through irreversible chemistry under mild conditions

Received: 3 September 2024

Accepted: 26 February 2025

Published online: 08 March 2025

Check for updates

Haoyong Yang[1], Junyi Han[1], Shengxu Li[1], Petko St. Petkov[2], Qunji Xue[1], Xinliang Feng[3,4] ✉ & Tao Zhang[1] ✉

Two-dimensional conjugated polymers (2DCPs) are a class of monolayer to multilayer crystalline polymeric materials with conjugated linkages at two-orthogonal directions that promise applications from membranes to electronics. Current interfacial synthesis methods have succeeded in constructing 2DCPs from dynamic covalent chemistry, e.g., imine linkages. However, these methods are unsuitable for fabricating the 2DCPs of robust olefin linkages due to the inadequate reversibility. Here we report the synthesis of 2DCPs linked by olefin bonds via amphiphilic-pyridinium-assisted aldol-type interfacial polycondensation. The synthesis is achieved by an alkyl-quaternized trimethylpyridine that can self-assemble into ordered monolayer at water interface and further react in situ with multifunctional aldehydes via aldol-type topologic polycondensation. The resultant 2DCPs show long-range molecular ordering, large lateral size and well-controlled thickness. Both experimental and theoretical analyses show that the pre-assembled trimethylpyridinium monolayer at water interface significantly boosts its condensation reactivity, thereby facilitating the synthesis of 2DCPs under mild conditions. The integration of the 2DCPs with inherent positive charges in an osmotic power generator gives excellent output power density reaching 51.4 W m^{-2}, superior to the most reported 2D nanoporous membranes.

Two-dimensional conjugated polymers (2DCPs), defined as mono- to multi-layer crystalline porous polymers[1,2], exhibit significant potential ranging from membranes to electronics due to their periodic conjugated frameworks and ordered nanopores[3–5]. To achieve such crystalline polymer materials, dynamic covalent chemistry is typically employed to allow reversible bond formation and structural self-correction[6,7]. So far, various interfacial synthesis methods have enabled the preparation of 2DCPs with reversible covalent bonds (e.g., C = N bond) at liquid interface[8,9] or on water surface[10,11]. Nevertheless, the inherent reversibility of these bonds sacrifices their structural chemical stability as well as application scope[12,13].

In contrast, recent advances have successfully constructed olefin-linked covalent organic frameworks (COFs) using irreversible chemistry under solvothermal conditions[14–16], which possess enhanced chemical stability and π-conjugation arising from the robust olefin linkage[17,18]. Such characteristics indeed render them as promising candidates for applications in electronic[19,20], catalysis[21,22] and membrane[23,24]. However, these polymers are typically obtained as insoluble powders and require harsh synthesis conditions[25,26]. This is

[1]State Key Laboratory of Advanced Marine Materials, Ningbo Institute of Materials Technology and Engineering, Chinese Academy of Sciences, Ningbo, China. [2]Faculty of Chemistry and Pharmacy, University of Sofia, Sofia, Bulgaria. [3]Department of Synthetic Materials and Functional Devices, Max Planck Institute of Microstructure Physics, Halle (Saale), Germany. [4]Center for Advancing Electronics Dresden (cfaed) and Faculty of Chemistry and Food Chemistry, Technische Universität Dresden, Dresden, Germany. ✉e-mail: xinliang.feng@tu-dresden.de; tzhang@nimte.ac.cn

because the existing interfacial synthesis methods for reversible chemistry are ineffective in synthesizing the 2DCPs with olefin linkages, due to the limited reversibility of the C = C bond[27].

In this work, we achieve the synthesis of crystalline olefin-linked 2DCP films via amphiphilic-pyridinium-assisted aldol-type interfacial polycondensation (AP-ATIP). The amphiphilic trimethylpyridine monomer, synthesized via alkyl-quaternization, can self-assemble into ordered monolayer at water interface. Subsequently, it undergoes in-situ aldol-type polycondensation reaction with aldehyde monomers to form crystalline 2DCP films on the water surface. The resultant 2DCPs feature with long-range molecular ordering, charged skeleton, robust C = C linkage, and ultrathin thickness (< 25 nm), and when applied in an osmotic energy generator, the 2DCPs exhibit a cation selectivity coefficient (*S*) of 0.68 and output power density reaching 51.4 W m^{-2} under harsh condition (pH = 3.5).

Results

Synthesis methodology

Initially, a series of amphiphilic N-alkyl-2,4,6-trimethylpyridinium (ATMP) monomers were prepared through one-step alkyl quaternization, where the methyl substituents can be activated to conduct aldol-type polycondensation with aldehydes to construct olefin linkage (Fig. 1a and Supplementary Section 2)[28,29]. Due to the long-alkyl substituent, the N-hexadecyl-2,4,6-trimethylpyridinium (HeTMP) exhibit representative self-assembly behavior in Langmuir-Blodgett (LB) trough, similar to surfactants of sodium oleyl sulfate (SOS) (Supplementary Fig. 2)[30]. To examine the interfacial synthetic feasibility, ATMP monomers were spread onto the water surface and then 2,5-dihydroxyterephthalaldehyde (DhTPA) and trifluoroacetic acid were injected to the water subphase to trigger the aldol-type interfacial polycondensation (Fig. 1b, c and Supplementary Fig. 3). Thin layer 2DCPs were then obtained after keeping the reaction at 80 °C for 2 days (Supplementary Figs. 4 and 5). Due to the inherent self-assembly capabilities, long-alkyl-substituted ATMP monomers demonstrated enhanced chemical reactivity (Fig. 1d, e), enabling the formation of homogeneous 2DCPs[10,31]. Furthermore, the controlled synthesis of 2DCP in aqueous interfacial systems was investigated (Supplementary Fig. 6), demonstrating that the enhanced reactivity of HeTMP enables the formation of free-standing films at ambient temperature (Supplementary Section 4.1). Compared with short alkyl-substituted monomers, the 2DCP thin films prepared via DTMP and HeTMP exhibit superior continuity and homogeneity, revealing the critical role of long-alkyl substituents in enhancing reactivity (Supplementary Section 4.2)[32,33].

Reaction mechanism of the AP-ATIP strategy

To gain insight to the enhancement of chemical reactivity and reaction mechanism (Fig. 2a), the interfacial self-assembly behaviors of ATMP were characterized through dynamic interfacial tension (IFT), small angle X-ray scattering (SAXS) and theoretical analysis. Representatively, the lowest interfacial tension was observed at a HeTMP concentration of 1 mM, arising from the formation of self-assembled structure (Fig. 2b and Supplementary Fig. 15)[34]. Laboratory SAXS analysis provided information of HeTMP on inducing a self-assembled structure, which in turn resulted in the formation of vesicle products (Supplementary Figs. 16–18)[35]. Molecular dynamics (MD) simulation was further utilized to provide an atom-level insight into the monolayer structure of ATMP monomers (Fig. 2c and Supplementary Fig. 19). The snapshot and number density profile of the equilibrated DTMP monolayer presented a preferential molecular orientation at the water/o-DCB interface, in alignment with the experimental findings (Fig. 2d, e). Furthermore, the calculated adsorption energy revealed the energetically favorable transport of 2,3,5,6-tetrafluoroterephthalaldehyde (TFT) and 4,4′,4″-(1,3,5-triazine-2,4,6-triyl) tribenzaldehyde (TFPT) molecules towards the ATMP monolayer,

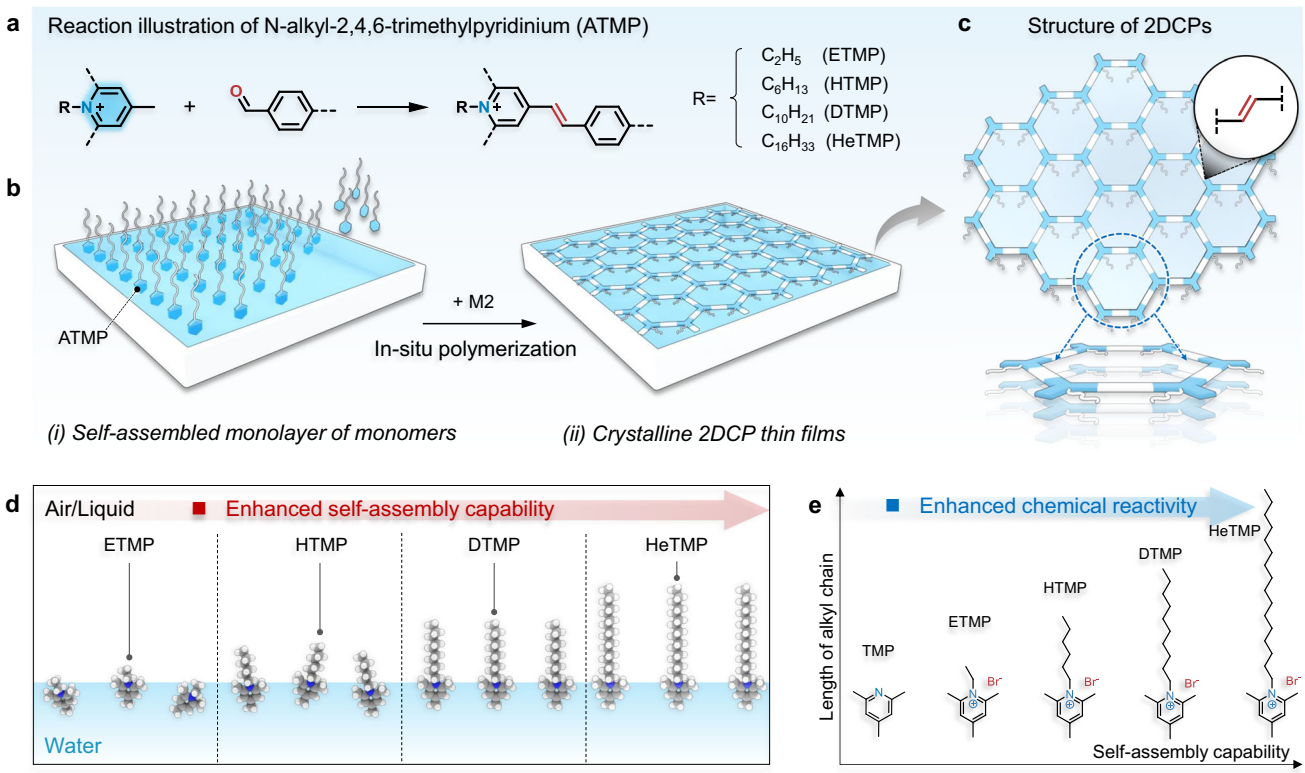

Fig. 1 | Amphiphilic-pyridinium-assisted aldol-type interfacial polycondensation (AP-ATIP). a Schematic of the reaction between ATMP and aldehyde monomer. **b** The synthesis of 2DCPs at air/water interface. **c** The structure of monolayer and multilayer 2DCPs. **d** The self-assembled monolayer of ATMP monomers at water interface. **e** The relationships of self-assembly capability and chemical reactivity among different ATMP monomers.

https://doi.org/10.1038/s41467-025-57612-0

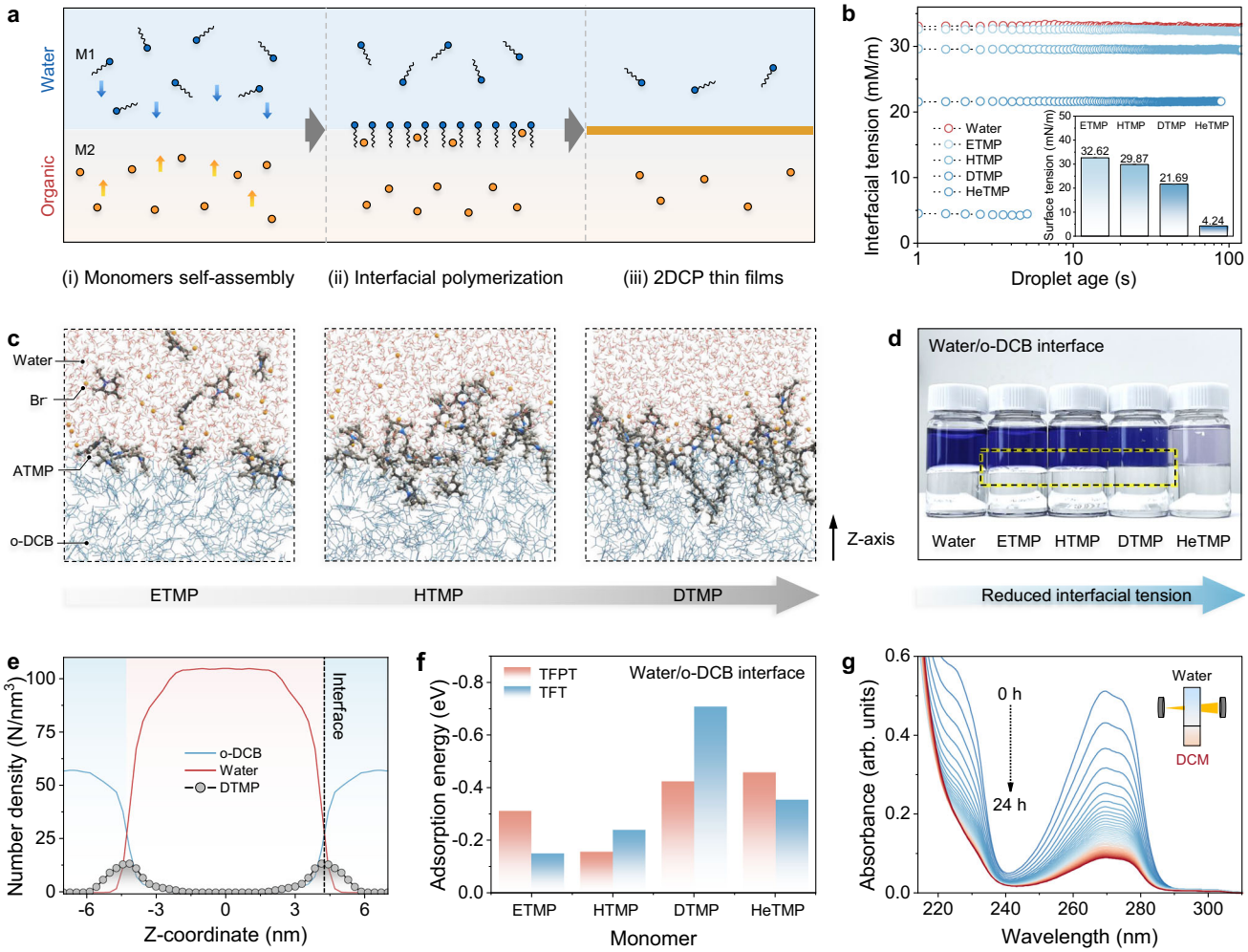

Fig. 2 | Reaction mechanism of AP-ATIP. a Schematic of aldol-type interfacial polymerization. **b** Plot of interfacial tension for ATMP monomers. Inset: the histogram of interfacial tension. **c** Molecular dynamics snapshot of the water/o-DCB interface with ETMP, HTMP and DTMP monomer, respectively. **d** The optical image of water/o-DCB interface with ATMP monomers. **e** Distribution of the DTMP along the normalized z distance obtained by MD simulation. **f** Adsorption energy between TFPT/TFT and ATMP monolayers. **g** In-situ UV-vis absorption spectra of HeTMP monomer at aqueous phase.

which facilitated the aldol-type interfacial polycondensation (Fig. 2f and Supplementary Figs. 20–23).

Accordingly, in-situ UV-vis absorption spectra revealed the rapid and spatially uniform diffusion of HeTMP monomer, enabling the continuous formation of 2DCPs in both time and space (Fig. 2g and Supplementary Figs. 24 and 25)[36]. Compared with water/dichloromethane (DCM) or water/chloroform (TCM) interfaces, the water/o-DCB interface greatly reduces the variance between monomer diffusion and interfacial reaction, as evidenced by the uniform change of absorbance change and morphology of resultant films (Supplementary Fig. 26). Through experimental and theoretical studies, we demonstrated that the feasibility of this protocol originates from the pro-organization of ATMP with self-assembled monolayer[37], which facilitates the accumulation of aldehyde monomers and accelerates the aldol-type interfacial polycondensation under mild conditions[38,39].

Synthesis of monolayer to multilayer 2DCPs

With a deep understanding of the interfacial growth mechanism, we have further achieved the controlled synthesis of 2DCP films with an optimized synthetic procedure at both air/water and water/o-DCB interface. The monolayer DTMP-TFT was synthesized via DTMP and 2,3,5,6-tetrafluoroterephthalaldehyde (TFT) under ambient conditions in the presence of 4-dimethylaminopyridine (DMAP) (Fig. 3a). The morphology of monolayer DTMP-TFT was characterized by optical microscopic (OM) and atomic force microscopy (AFM). A uniform and continuous monolayer DTMP-TFT was obtained at air/water interface (Fig. 3b), whereas the monolayer DTMP-TFT formed at water/o-DCB interface exhibited wrinkling after transferred (Fig. 3g inset and Supplementary Fig. 27). AFM image reveals a smooth surface and thickness of ~1.0 nm, near the expected thickness of a monolayer (Fig. 3c–f). The defined thickness of DTMP-TFT can be achieved from 7.4 nm to 21.2 nm by extending the synthesis time from 5 to 60 min at water/o-DCB interface (Fig. 3g and Supplementary Fig. 28). The lateral size of film could be scaled up to wafer size (~20 cm^2) at air/water interface (Fig. 3h). After transferred onto a copper grid, a 3.4 nm thick film was freely suspended over the mesh with a considerable length to aspect ratio of 10^3, suggesting its high mechanical stiffness (Fig. 3i and Supplementary Fig. 29). The transmission electron microscopy (TEM) images further demonstrated a uniform and stacked area of DTMP-TFT (Fig. 3j and Supplementary Fig. 30).

Structural characterizations of 2DCPs

To evaluate the chemical and crystal structure, various multilayer 2DCP films were prepared at water/o-DCB interface using DTMP in combination with TFT, DhTPA, TFPT and 3,3′-dihydroxy-[1,1′-biphenyl]−4,4′-dicarbaldehyde (DhBDA), named as DTMP-TFT, DTMP-DhTPA, DTMP-TFPT and DTMP-DhBDA, respectively (Fig. 4a). The morphology characterization of these films was detailed in Supplementary

https://doi.org/10.1038/s41467-025-57612-0

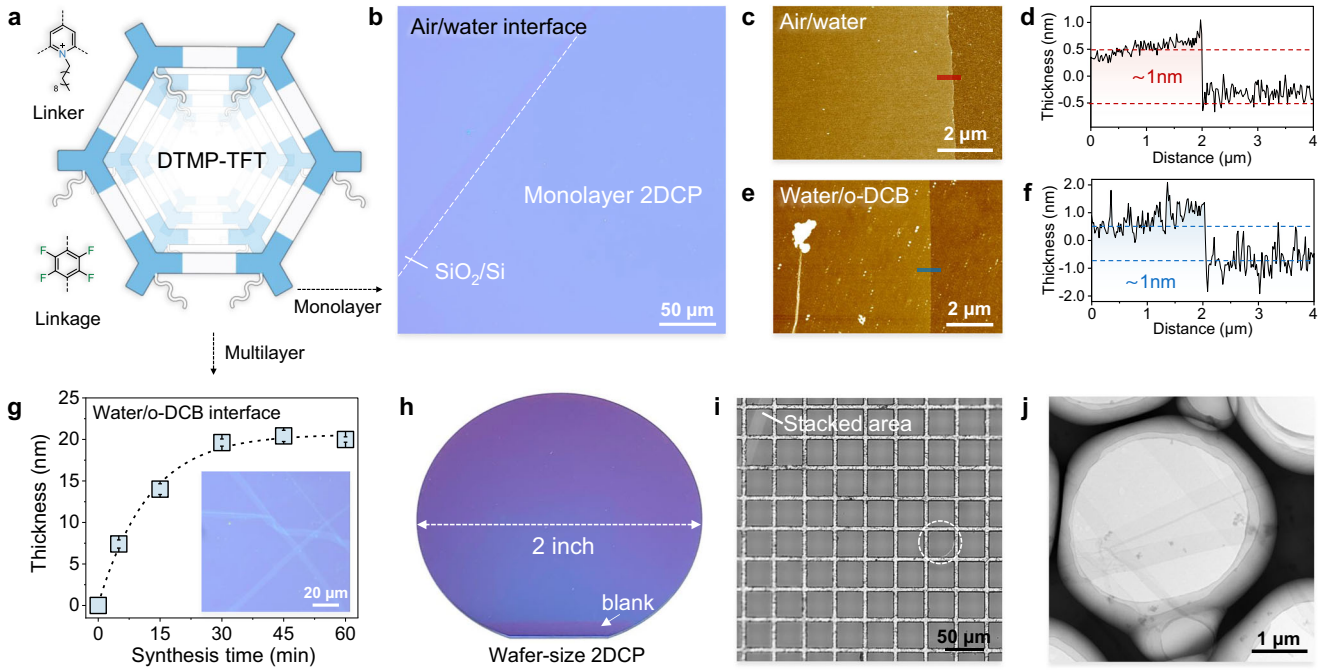

Fig. 3 | Morphological charaterization of the 2DCPs. a Schematic of monolayer and multilayer DTMP-TFT. **b** Optical image of the monolayer DTMP-TFT fabricated at air/water interface. AFM image (**c**) and height analysis (**d**) of the monolayer DTMP-TFT fabricated at air/water interface. AFM image (**e**) and height analysis (**f**) of the monolayer DTMP-TFT fabricated at water/o-DCB interface. **g** Thickness of DTMP-TFT *vs* synthesis time from 5 to 60 min under R.T. Inset: monolayer DTMP-TFT fabricated at water/o-DCB interface. The sample size (n) of the experimental group is $n = 5$, and the error bars represent the variations in thickness measurement at three different positions on each 2DCP sample. **h** The 2DCPs on a 2-inch SiO_2/Si wafer. **i** Optical image of the multilayer DTMP-TFT suspended on a copper grid. **j** TEM image of DTMP-TFT.

Section 7.1. Fourier transform infrared spectroscopy (FTIR) revealed that the peak at 970 cm^{-1} assigned to the trans-C = C stretch vibration had newly appeared, indicating the successful formation of olefin linkage (Fig. 4b and Supplementary Fig. 43)[40]. Furthermore, 2DCP thin films were soaked in 6 M HCl and 6 M NaOH solutions for 48 h and the FT-IR spectra indicated good chemical stability under harsh conditions (Supplementary Fig. 44). Solid-state nuclear magnetic resonance (NMR) spectroscopy revealed that the peak signals located at 127, 135 and 145 ppm originated from the carbon atoms of olefin linkages and benzene rings, and the signal appearing between 52 and 14 ppm can be attributed to the alkyl chain (Fig. 4c, d and Supplementary Fig. 45). In X-ray photoelectron spectroscopy (XPS) spectra, the O 1*s* peak at ~530.5 eV can be assigned to the C-O bond from DhTPA and the F 1*s* peak at ~687.8 eV can be attributed to the C-F bond from TFT (Supplementary Fig. 46). The deconvoluted N 1*s* XPS spectra further showed two types of nitrogen of pyridinium N (~401.6 eV) from DTMP and triazine N (~398.9 eV) from TFPT[40].

The grazing incidence wide-angle X-ray scattering (GIWAXS) data of DTMP-DhBDA showed that the diffraction signal at $Q_{xy} = 0.35$ $Å^{-1}$ correspond to the [100] reflection plane with a 2θ value of 3.8° (Fig. 4e, f), which was well consistent with the simulated AA stacking mode with a hexagonal lattice with a = 29.84 Å, b = 31.14 Å and γ = 120° (Supplementary Fig. 47). In addition, the diffraction projections of DTMP-TFT at 4.7° indicated the extended crystalline structure, which was agreement with the eclipsed AA stacking mode with a hexagonal lattice with a = 23.59 Å, b = 23.25 Å and γ = 122.4° (Fig. 4g and Supplementary Figs. 48 and 49). Laboratory SAXS analysis shows that the DTMP-TFT films catalyzed by acid or base exhibit a similar degree of crystallinity (Supplementary Fig. 50)[41,42]. The weakened crystallinity of 2DCP thin film and powder probably originates from the fact that the long alkyl chain affects the stacking and crystallizing process (Supplementary Fig. 51). When the alkyl chain and resulted chemical reactivity increase, the 2DCPs will generate structural transformation to balance the in-plane and out-plane structures, as confirmed by the structural characterization of HeTMP-based 2DCP thin films and powders (Supplementary Figs. 52–55).

Osmotic energy conversion

Owing to the charged robust skeleton and ultrathin thickness, the homogeneous 2DCP films fabricated via DTMP were applied in an osmotic power generator to achieve high performance energy conversion, including DTMP-DhTPA and DTMP-TFPT thin films (Fig. 5a). A multilayer DTMP-DhTPA film with thickness of 22 nm was transferred onto a silicon wafer with an open hole of about 6.25 $μm^2$. The transmembrane ionic transport property was evaluated in potassium chloride (KCl) solution with standard saturated Ag/AgCl salt bridge electrodes. The transmembrane conductivities showed saturation at low salt concentrations at pH = 3.5, which suggests a charge-governed ion transport of DTMP-DhTPA film (Fig. 5b, Inset). The permselectivity of DTMP-DhTPA film was investigated in KCl concentration gradient system. Due to ion-selective accumulation, the osmotic potential (V_{os}) exhibited an increasing and then a decreasing trend versus the concentration gradient (C_H/C_L), while the positive osmotic current (I_{os}) increased from 22 to 47 nA, demonstrating a cation selectivity at pH = 3.5 (Fig. 5c)[43]. In contrast, the DTMP-TFPT film with thickness of 12 nm exhibits anion selectivity due to the protonation of pyridine nitrogen (Supplementary Fig. 56). Furthermore, the ion selectivity coefficient (*S*) of DTMP-DhTPA film was calculated as 0.68 under 50-fold KCl concentration gradient (Supplementary Fig. 57), outperforming the previously reported ultrathin organic and inorganic materials such as single-layer MoS_2 and holey-graphene-like membranes (0.4)[44,45]. The osmotic power-generation performance was further evaluated under various ionic concentrations and pH conditions and the harvested osmotic power, calculated as $P_{max} = I^2R$, was observed to be pH dependent. Under 50-fold NaCl salinity gradient, the output power density of DTMP-TFPT film reached 16.9 W m^{-2} at pH = 3.5 with long term stability (Supplementary Figs. 58 and 59). In contrast, the output power density of DTMP-DhTPA film achieved a maximum value of 51.4 W m^{-2} at pH =

https://doi.org/10.1038/s41467-025-57612-0

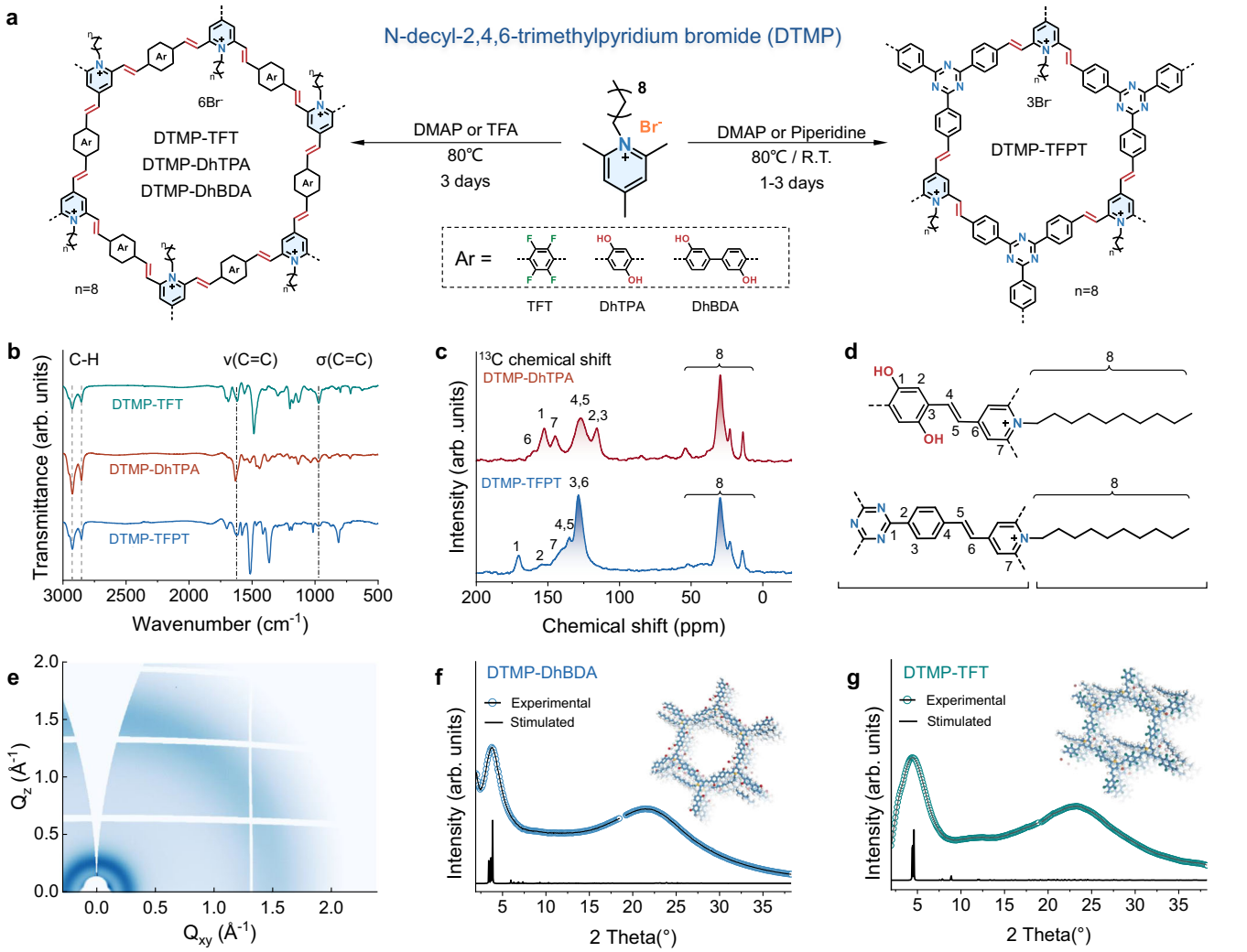

Fig. 4 | Structural charaterization of the 2DCP films. a Synthesis protocol of 2DCPs. **b** FTIR spectra of 2DCP films. Solid-state ^{13}C NMR spectra (**c**) and molecular structure (**d**) of 2DCP films. **e** GIWAXS pattern of DTMP-DhBDA film. Projections of GIWAXS data of DTMP-DhBDA film (**f**) and DTMP-TFT film (**g**).

3.5 (Fig. 5d and Supplementary Figs. 60 and 61). As such, the DTMP-DhTPA film demonstrated an output power of 51.4 W m^{-2} with high stability under harsh conditions (Fig. 5e), which outperforms the most reported membranes (Fig. 5f and Supplementary Table 2).

Discussion

In summary, we report the synthesis of crystalline olefin-linked 2DCP films via amphiphilic-pyridinium-assisted aldol-type interfacial polycondensation. The resultant 2DCPs demonstrate long-range molecular ordering, wafer-scale homogeneity (~20 cm^2) and well controllable thickness from monolayer to multilayer (~1.0–21.2 nm). Due to the inherent charged skeletons and enhanced chemical stability, in an osmotic power generator, the 2DCP film shows high-performance osmotic energy generation of 51.4 W m^{-2} under harsh working conditions at pH = 3.5. Our approach provides the possibility for the large-scale fabrication of thickness-controlled 2DCP thin films with full conjugated linkage that exhibit great potential from membrane technology to future thin-film organic electronics.

Methods

Chemicals and materials

Mesitylene (97%), orthodichlorobenzene (99%), 2,4,6-trimethylpyridine (99%), ethyl bromide (99%), hexyl bromide (99%), decyl bromide (98%), hexadecyl bromide (97%), trifluoroacetic acid (99.0%) and dimethylaminopyridine (99%) were purchased from Shanghai Aladdin Biochemical Technology Co., Ltd. Dichloromethane (99.5%), chloroform (99%), piperidine (99%) were purchased from Sinopharm Chemical Reagent Co., Ltd. 3,3'-dihydroxy-[1,1'-biphenyl]−4,4'-dicarbaldehyde (97%), 4,4',4''-(1,3,5-triazine-2,4,6-triyl)tribenzaldehyde (97%), 2,3,5,6-tetrafluoroterephthalaldehyde (98%), 2,5-dihydroxyterephthalaldehyde (95%) were purchased from Bide Pharmatech Co., Ltd. Solvents were obtained from commercial sources and used without further purification.

Synthesis of 2DCPs at air/water interface

A static air/water interface was formed in a beaker (80 mL, diameter = 6 cm) by injecting 40 mL of Milli-Q water. Then, 10 μL of ATMP monomer (1 mg mL^{-1} in chloroform) was spread onto the surface and allowed to evaporate for 30 min. Afterwards, 1.6 μmol of DhTPA monomer in 0.12 M HCl aqueous solution was gently added to the subphase using a syringe. After 30 min, 5 μl of trifluoroacetic acid was injected into the subphase. The reaction mixture was kept undistracted at 80 °C for 2 days. After a vertical transfer of the resulting 2DCP films onto 300 nm SiO_2/Si wafer, optical microscopy (OM) and atomic force microscopy (AFM) were performed to study the morphology of the film.

https://doi.org/10.1038/s41467-025-57612-0

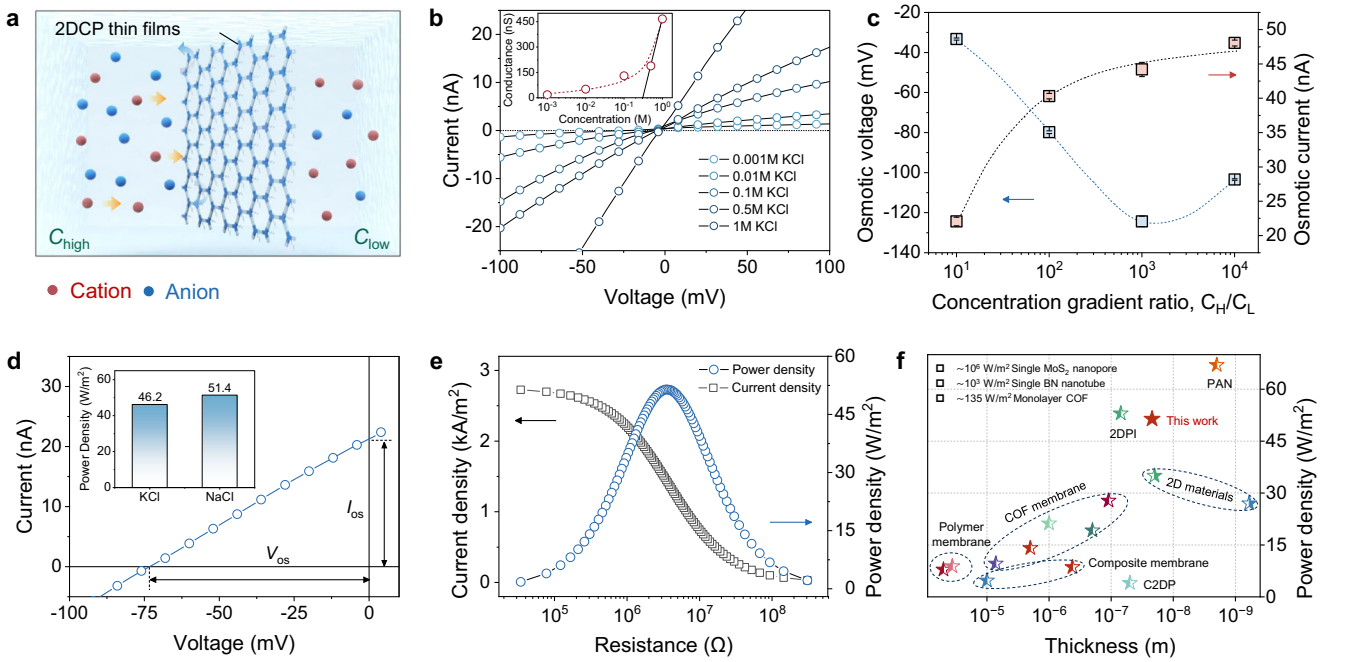

Fig. 5 | Osmotic energy conversion. a Schematic of the selective ion transport through 2DCPs. **b** The I–V curves of the DTMP-DhTPA film in KCl solution at pH = 3.5. Inset: conductance measurement of film under different KCl concentrations. **c** Osmotic current and osmotic voltage in various KCl salinity gradients. The sample size (n) of the experimental is $n = 1$, and the error bars are standard deviations with three independent experiments. **d** I–V curves of the DTMP-DhTPA film recorded under 0.5/0.01 M NaCl of pH = 3.5. Inset: comparison of the output power density in KCl and NaCl with concentration gradient of 50 at pH = 3.5. **e** Current density and output power density depend on the external load resistance in 0.5/0.01 M NaCl. **f** Comparison of the osmotic energy generation performance of the DTMP-DhTPA film with previously reported results, except for single MoS_2 nanopore, single BN nanotube, and monolayer COF. Corresponding membranes were shown in Supplementary Table 2.

Synthesis of 2DCPs at liquid/water interface

The aldehyde monomer was dissolved in 5 mL bottom solution (e.g., orthodichlorobenzene/dichloromethane/chloroform) and then added into a vial (20 mL volume, 2 cm diameter). Then, 5 mL ATMP aqueous solution (1 mM) was added slowly to the bottom solution along the glass bottle wall to leave a clear and stable interface. The interfacial system was placed in a vibration-free environment under ambient conditions for 30 min. After the formation of pre-assembled ATMP monolayer at the interface, 5 μL of a catalyst (e.g., piperidine, trifluoroacetic acid) was slowly added to the aqueous layer along the wall of vial using a syringe. Then, the vial was capped and placed in vibration free environment at room temperature or 80 °C. After the reaction was completed, the film was transferred to target substrates and further washed with acetone, tetrahydrofuran, and Milli-Q water.

Isotherm of HeTMP monomer

A Langmuir-Blodgett trough (Minitrough, KSV NIMA, Finland) equipped with a platinum Wilhelmy plate, a taflon dipper and a pair of delrin barriers, was used to measure the surface pressure-mean molecular area (π-A) isotherm of HeTMP. Chloroform solution of the HeTMP (1 mg mL^{-1}) was firstly spread on the water surface with a microsyringe. After 30 minutes, when the solvent was evaporated, the π-A isotherm was recorded at a continuous pressing speed for the barrier of 1 mm min^{-1} at room temperature.

Reaction kinetics analysis

To gain insight to the kinetics of the interfacial polymerization, the absorption percentage of monomer in aqueous phase was monitored by in-situ UV-vis spectra to simulate the HeTMP monomer transfer process during the experiment. Typically, orthodichlorobenzene (o-DCB) solution of TFPT monomer was place on the bottom of the cuvette and then a certain amount of water solution of HeTMP monomer was place on the upper layer of o-DCB solvent to simulate the actual reaction conditions. Then, the absorbance change of the aqueous solution was recorded to analyse the HeTMP monomer mass transfer process under room temperature and atmospheric pressure. To determine the role of interfacial mass transfer, we compared the interfacial reaction kinetics of HeTMP monomer in different solvent systems (e.g., water/mesitylene (TMB); water/dichloromethane (DCM); water/chloroform (TCM)).

Osmotic energy harvest

The current–voltage (I–V) measurements and energy conversion tests were performed with an Keithley 2646B source meter (Keithley Instruments). The as-prepared 2DCP film was transferred onto a silicon wafer containing an open hole of about 6.25 μm^2 and was further mounted between a two-compartment conductivity cell. Standard electrodes (saturated Ag/AgCl salt bridge electrodes) were used to measure the resulting current. The 2DCP film was clamped in the electrochemical cell and stayed in the testing solutions all the time, and the testing solutions were replenished before each measurement. The KCl was selected as the standard electrolyte because of the close diffusion coefficients of K^+ and Cl^- ions, while the NaCl electrolyte was selected to imitate the river water and seawater.

The ion selectivity coefficient (S) is defined as (t_+-t_-), where the t_+ and t_- are the ion transference number of cation and anion, respectively. Under a concentration gradient, the recorded osmotic potential (V_{os}) can be described as:

$$V_{os} = S\frac{RT}{F}\ln\left(\frac{c_H}{c_L}\right)$$

where R, T and F are the universal gas constant, absolute temperature and Faraday constant, respectively. c is the concentration of electrolyte solution in the high-concentration (H) and low-concentration (L) sides.

Computational simulations

The Gaussian 16 software program was used to obtain the Hessian matrix of ATMP and o-DCB at B3LYP(D3) method[46] with 6-311 (d,p) basis set[47]. And all atoms performed Restrained Electrostatic Potential (RESP)[48] atomic charge. All MD simulations were performed using GROMACS software[49] to provide an atom-level insight of self-assembly structures of ATMP at the interface. Four MD systems were constructed with different self-assembly AMTP monolayers at the water/o-DCB interface. The systems were comprised of the same numbers of H_2O (5000), ATMP monomers (18) and o-DCB (400) in a rectangular box ($50 \times 50 \times 140$ Å^3). Initial structures for molecular dynamic simulation were constructed by the Packmol software package[50]. Parameters of the atomistic models based on the GAFF force field. Three-dimensional periodic boundary conditions (PBC) were used to avoid the influence of the box boundary during simulation. The cut-off distance of non-bonded interactions is 10 Å, and the long-range electrostatic interactions were calculated by the particle-mesh Ewald (PME) method. Before the dynamics simulation, the steepest descent algorithm was used to pre-equalize the system for eliminating the excessive stress in initial structures. After pre-equilibrium, a 20-ns production simulation under NPT ensemble with a time-step of 2 fs was carried out for data collection. Temperature and pressure coupling was performed using v-rescale thermostat[51] and Berendsen barostat[52] at 298 K and 1 atm. The trajectories were used for post-analysis and visualized by visual molecular dynamics (VMD) 1.9.3[53]. The relative concentrations of water, o-DCB and ATMP along the Z distance were obtained by MD simulation. After MD relaxation, we obtained an equilibrated ATMP monomers distribution at water/o-DCB interface.

To further explore the interaction between ATMP monolayer and aldehyde monomers, we calculated the adsorption energy ($E_{adsorption}$) of an TFPT or TFT molecular at different positions in the water/o-DCB system: o-DCB bulk solution and water/o-DCB interface.

$$E_{adsorption} = E_{system} - E_{ATMP} - E_{CHO}$$

where E_{system} is the total energy of the system including the aldehyde monomer and ATMP monolayer, E_{CHO} is the energy of system with one TFPT or TFT molecular, and E_{ATMP} is the energy of the system with ATMP monolayer, respectively. The negative binding energy usually indicates an energetically favorable adsorption between the adsorbate and the target surface. The presence of ATMP monolayer facilitate the transport of TFPT/TFT molecule from the o-DCB phase to the interface, thus elevated the TFPT/TFT concentration at the water/o-DCB interface and enhanced the interfacial polymerization.

Since the structure of the 2DCPs is rather large, we applied SCC-DFTB approach to find the most suitable atomistic monolayer and multilayer models. For this purpose, a DFTB+ software[54] was used with 3ob-3-1 parameter set[55]. The experimental guess for the 3D models was fully optimized (cell and lattice vectors) at SCC-DFTB level. After detailed comparison with the experimental GIWAXS patterns and simulated XRD patterns of all models, the most appropriate multilayered model was selected for further analysis.

Data availability

All data supporting the findings of this study are available within the article and the Supplementary Information file. Source data are provided with this paper. Additional data are available from the corresponding authors upon request. Source data are provided with this paper.

References

1. Wang, M. et al. Exceptionally high charge mobility in phthalocyanine-based poly(benzimidazobenzophenanthroline)-ladder-type two-dimensional conjugated polymers. *Nat. Mater.* **22**, 880–887 (2023).
2. Tan, K. T. et al. Covalent organic frameworks. *Nat. Rev. Methods Primers* **3**, 1–19 (2023).
3. Jing, Y. & Heine, T. Two-dimensional kagome lattices made of hetero triangulenes are dirac semimetals or single-band semiconductors. *J. Am. Chem. Soc.* **141**, 743–747 (2019).
4. Galeotti, G. et al. Synthesis of mesoscale ordered two-dimensional π-conjugated polymers with semiconducting properties. *Nat. Mater.* **19**, 874–880 (2020).
5. Evans, A. M. et al. Two-dimensional polymers and polymerizations. *Chem. Rev.* **122**, 442–564 (2022).
6. Colson, J. W. & Dichtel, W. R. Rationally synthesized two-dimensional polymers. *Nat. Chem.* **5**, 453–465 (2013).
7. Zhan, G. et al. Observing polymerization in 2D dynamic covalent polymers. *Nature* **603**, 835–840 (2022).
8. Zhong, Y. et al. Wafer-scale synthesis of monolayer two-dimensional porphyrin polymers for hybrid superlattices. *Science* **366**, 1379–1384 (2019).
9. Yang, J. et al. Advancing osmotic power generation by covalent organic framework monolayer. *Nat. Nanotechnol.* **17**, 622–628 (2022).
10. Liu, K. et al. On-water surface synthesis of crystalline, few-layer two-dimensional polymers assisted by surfactant monolayers. *Nat. Chem.* **11**, 994–1000 (2019).
11. Yang, Y. et al. Elastic films of single-crystal two-dimensional covalent organic frameworks. *Nature* **630**, 878–883 (2024).
12. Haase, F. & Lotsch, B. V. Solving the COF trilemma: towards crystalline, stable and functional covalent organic frameworks. *Chem. Soc. Rev.* **49**, 8469–8500 (2020).
13. Zhang, W. et al. Reconstructed covalent organic frameworks. *Nature* **604**, 72–79 (2022).
14. Jin, E. et al. Two-dimensional sp^2 carbon-conjugated covalent organic frameworks. *Science* **357**, 673–676 (2017).
15. Lyu, H., Diercks, C. S., Zhu, C. & Yaghi, O. M. Porous crystalline olefin-linked covalent organic frameworks. *J. Am. Chem. Soc.* **141**, 6848–6852 (2019).
16. Pastoetter, D. L. et al. Synthesis of vinylene-linked two-dimensional conjugated polymers via the Horner–Wadsworth–Emmons reaction. *Angew. Chem. Int. Ed.* **59**, 23620–23625 (2020).
17. Liu, R. et al. Linkage-engineered donor–acceptor covalent organic frameworks for optimal photosynthesis of hydrogen peroxide from water and air. *Nat. Catal.* **7**, 195–206 (2024).
18. Fu, G. et al. Construction of thiadiazole-bridged sp^2 -carbon-conjugated covalent organic frameworks with diminished excitation binding energy toward superior photocatalysis. *J. Am. Chem. Soc.* **146**, 1318–1325 (2024).
19. Bi, S. et al. Two-dimensional semiconducting covalent organic frameworks via condensation at arylmethyl carbon atoms. *Nat. Commun.* **10**, 2467 (2019).
20. Li, Y.-J. et al. A general design approach toward covalent organic frameworks for highly efficient electrochemiluminescence. *Nat. Commun.* **12**, 4735 (2021).
21. Li, S. et al. Direct construction of isomeric benzobisoxazole–vinylene-linked covalent organic frameworks with distinct photocatalytic properties. *J. Am. Chem. Soc.* **144**, 13953–13960 (2022).
22. Teng, Z. et al. Atomically isolated $Sb(CN)_3$ on sp^2-c-COFs with balanced hydrophilic and oleophilic sites for photocatalytic C-H activation. *Sci. Adv.* **10**, eadl5432 (2024).

23. Liang, B. et al. Microporous membranes comprising conjugated polymers with rigid backbones enable ultrafast organic-solvent nanofiltration. *Nat. Chem.* **10**, 961–967 (2018).
24. Shen, J. et al. Fast water transport and molecular sieving through ultrathin ordered conjugated-polymer-framework membranes. *Nat. Mater.* **21**, 1183–1190 (2022).
25. Wang, Z. et al. Green synthesis of olefin-linked covalent organic frameworks for hydrogen fuel cell applications. *Nat. Commun.* **12**, 1982 (2021).
26. Wang, Y. et al. Facile construction of fully sp^2-carbon conjugated two-dimensional covalent organic frameworks containing benzobisthiazole units. *Nat. Commun.* **13**, 100 (2022).
27. Xu, S., Richter, M. & Feng, X. Vinylene-linked two-dimensional covalent organic frameworks: synthesis and functions. *Acc. Mater. Res.* **2**, 252–265 (2021).
28. Zhang, P. et al. Fabricating industry-compatible olefin-linked COF resins for oxoanion pollutant scavenging. *Angew. Chem. Int. Ed.* **61**, e202213247 (2022).
29. Meng, F. et al. Synthesis of ionic vinylene-linked covalent organic frameworks through quaternization-activated Knoevenagel condensation. *Angew. Chem. Int. Ed.* **60**, 13614–13620 (2021).
30. Zhang, T. et al. Engineering crystalline quasi-two-dimensional polyaniline thin film with enhanced electrical and chemiresistive sensing performances. *Nat. Commun.* **10**, 4225 (2019).
31. Yang, Y. et al. On-water surface synthesis of vinylene-linked cationic two-dimensional polymer films as the anion-selective electrode coating. *Angew. Chem. Int. Ed.* **63**, e202316299 (2024).
32. Liang, Y. et al. Polyamide nanofiltration membrane with highly uniform sub-nanometre pores for sub-1 Å precision separation. *Nat. Commun.* **11**, 2015 (2020).
33. Shen, Q. et al. When self-assembly meets interfacial polymerization. *Sci. Adv.* **9**, eadf6122 (2023).
34. Peng, Q. et al. Extreme Li-Mg selectivity via precise ion size differentiation of polyamide membrane. *Nat. Commun.* **15**, 2505 (2024).
35. Chen, X. et al. Hydrocarbon degradation by contact with anoxic water microdroplets. *J. Am. Chem. Soc.* **145**, 21538–21545 (2023).
36. Giri, A., Shreeraj, G., Dutta, T. K. & Patra, A. Transformation of an imine cage to a covalent organic framework film at the liquid–liquid interface. *Angew. Chem. Int. Ed.* **62**, e202219083 (2023).
37. Prasoon, A. et al. Site-selective chemical reactions by on-water surface sequential assembly. *Nat. Commun.* **14**, 8313 (2023).
38. Ruiz-Lopez, M. F., Francisco, J. S., Martins-Costa, M. T. C. & Anglada, J. M. Molecular reactions at aqueous interfaces. *Nat. Rev. Chem.* **4**, 459–475 (2020).
39. Kusaka, R., Nihonyanagi, S. & Tahara, T. The photochemical reaction of phenol becomes ultrafast at the air–water interface. *Nat. Chem.* **13**, 306–311 (2021).
40. Zhang, Z. & Xu, Y. Hydrothermal synthesis of highly crystalline zwitterionic vinylene-linked covalent organic frameworks with exceptional photocatalytic properties. *J. Am. Chem. Soc.* **145**, 25222–25232 (2023).
41. Jing, X. et al. Gradient channel segmentation in covalent organic framework membranes with highly oriented nanochannels. *J. Am. Chem. Soc.* **145**, 21077–21085 (2023).
42. Pelkowski, C. E. et al. Tuning crystallinity and stacking of two-dimensional covalent organic frameworks through side-chain interactions. *J. Am. Chem. Soc.* **145**, 21798–21806 (2023).
43. Chen, S. et al. Imparting ion selectivity to covalent organic framework membranes using de novo assembly for blue energy harvesting. *J. Am. Chem. Soc.* **143**, 9415–9422 (2021).
44. Feng, J. et al. Single-layer MoS_2 nanopores as nanopower generators. *Nature* **536**, 197–200 (2016).
45. Liu, X. et al. Power generation by reverse electrodialysis in a single-layer nanoporous membrane made from core-rim polycyclic aromatic hydrocarbons. *Nat. Nanotechnol.* **15**, 307–312 (2020).
46. Stephens, P. J., Devlin, F. J., Chabalowski, C. F. & Frisch, M. J. Ab initio calculation of vibrational absorption and circular dichroism spectra using density functional force fields. *J. Phys. Chem.* **98**, 11623–11627 (1994).
47. Ditchfield, R., Hehre, W. J. & Pople, J. A. Self-consistent molecular-orbital methods. IX. An extended gaussian-type basis for molecular-orbital studies of organic molecules. *J. Chem. Phys.* **54**, 724–728 (1971).
48. Bayly, C. I., Cieplak, P., Cornell, W. & Kollman, P. A. A well-behaved electrostatic potential based method using charge restraints for deriving atomic charges: the RESP model. *J. Phys. Chem.* **97**, 10269–10280 (1993).
49. Abraham, M. J. et al. GROMACS: high performance molecular simulations through multi-level parallelism from laptops to supercomputers. *SoftwareX* **1–2**, 19–25 (2015).
50. Martínez, L., Andrade, R., Birgin, E. G. & Martínez, J. M. PACKMOL: a package for building initial configurations for molecular dynamics simulations. *J. Comput. Chem.* **30**, 2157–2164 (2009).
51. Bussi, G., Donadio, D. & Parrinello, M. Canonical sampling through velocity rescaling. *J. Chem. Phys.* **126**, 014101 (2007).
52. Berendsen, H. J. C., Postma, J. P. M., van Gunsteren, W. F., DiNola, A. & Haak, J. R. Molecular dynamics with coupling to an external bath. *J. Chem. Phys.* **81**, 3684–3690 (1984).
53. Humphrey, W., Dalke, A. & Schulten, K. VMD: visual molecular dynamics. *J. Mol. Graph.* **14**, 33–38 (1996).
54. Hourahine, B. et al. DFTB+, a software package for efficient approximate density functional theory based atomistic simulations. *J. Chem. Phys* **152**, 124101 (2020).
55. Gaus, M., Goez, A. & Elstner, M. Parametrization and benchmark of DFTB3 for organic molecules. *J. Chem. Theory Comput.* **9**, 338–354 (2013).

Acknowledgements

T.Z. acknowledges the National Natural Science Fund for Excellent Young Scholars (Grant No. 52322316), the Distinguished Youth Foundation of Zhejiang Provincial Natural Science Foundation of China (Grant No. LRG25E030001) and the Key Research and Development Program of Ningbo (Grant No. 2022ZDYF020023). This work was also supported by the User Experiment Assist System of Shanghai Synchrotron Radiation Facility (SSRF). H.Y. acknowledges Xuke Li for help with SAXS measurements. P.St.P. acknowledge the support from the European Union-NextGenerationEU, through the National Recovery and Resilience Plan of the Republic of Bulgaria, project No BG-RRP-2.004-0008.

Author contributions

H.Y. and T.Z. conceived and designed the experiments. H.Y. carried out most of the experiments. J.H. performed the molecular dynamic simulations. S.L. contributed to helpful discussion during experiments. P.St.P. implemented the crystal structure stimulations. T.Z., X.F. and Q.X. revised the manuscript and provided some suggestions. All authors discussed the results and commented on the manuscript.

Competing interests

T.Z. and H.Y. has applied for a patent for the amphiphilic-pyridinium-assisted aldol-type interfacial polycondensation strategy (CN202410515941.2). The remaining authors declare no competing interests.

Additional information

Supplementary information The online version contains supplementary material available at https://doi.org/10.1038/s41467-025-57612-0.

Correspondence and requests for materials should be addressed to Xinliang Feng or Tao Zhang.

Peer review information *Nature Communications* thanks Xiaobai Li and the other, anonymous, reviewers for their contribution to the peer review of this work. A peer review file is available.

Reprints and permissions information is available at http://www.nature.com/reprints

Publisher's note Springer Nature remains neutral with regard to jurisdictional claims in published maps and institutional affiliations.

Open Access This article is licensed under a Creative Commons Attribution-NonCommercial-NoDerivatives 4.0 International License, which permits any non-commercial use, sharing, distribution and reproduction in any medium or format, as long as you give appropriate credit to the original author(s) and the source, provide a link to the Creative Commons licence, and indicate if you modified the licensed material. You do not have permission under this licence to share adapted material derived from this article or parts of it. The images or other third party material in this article are included in the article's Creative Commons licence, unless indicated otherwise in a credit line to the material. If material is not included in the article's Creative Commons licence and your intended use is not permitted by statutory regulation or exceeds the permitted use, you will need to obtain permission directly from the copyright holder. To view a copy of this licence, visit http://creativecommons.org/licenses/by-nc-nd/4.0/.

© The Author(s) 2025